

# Néel-vector Control of Magnetization Dynamics in $\alpha$ -Fe<sub>2</sub>O<sub>3</sub>/NiFe Heterostructures

Hassan Al-Hamdo,<sup>1,\*</sup> Tobias Wagner,<sup>2,†</sup> Philipp Schwenke,<sup>1</sup> Gutenberg Kendzo,<sup>1</sup> Maximilian Dausend,<sup>1</sup> Laura Scheuer,<sup>1</sup> Misbah Yaqoob,<sup>1</sup> Vitaliy I. Vasyuchka,<sup>1</sup> Philipp Pirro,<sup>1</sup> Olena Gomony,<sup>2</sup> and Mathias Weiler<sup>1</sup>

<sup>1</sup>*Fachbereich Physik and Landesforschungszentrum OPTIMAS, Rheinland-Pfälzische Technische Universität Kaiserslautern-Landau, 67663 Kaiserslautern, Germany*  
<sup>2</sup>*Institute of Physics, Johannes Gutenberg-University Mainz, 55099 Mainz, Germany*

We investigate spin dynamics in  $\alpha$ -Fe<sub>2</sub>O<sub>3</sub>/Ni<sub>80</sub>Fe<sub>20</sub> (Py) heterostructures, uncovering a robust mechanism for in-situ modulation of ferromagnetic resonance (FMR) through precise control of temperature, applied magnetic field and crystal orientation. Employing cryogenic ferromagnetic resonance spectroscopy, we demonstrate that the interfacial coupling between the Néel vector of  $\alpha$ -Fe<sub>2</sub>O<sub>3</sub> and the magnetization of the Py layer is highly tunable across the Morin transition temperature ( $T_M$ ). Our experiments reveal distinct resonance behavior for different crystal orientations, highlighting the pivotal role of exchange coupling strength in dictating FMR frequencies. Theoretical modeling corroborates the experimental findings, elucidating the dependence of coupling on the relative alignment of the Néel vector and ferromagnetic magnetization. Notably, we achieve significant modulation of FMR frequencies by manipulating the Néel vector configuration, facilitated by temperature variations, applied magnetic fields and crystal orientation adjustments. These advancements demonstrate the potential for dynamic control of spin interactions in AFM/FM heterostructures, paving the way for the development of advanced spintronic devices with tunable magnetic properties. Our work provides critical insights into the fundamental interactions governing hybrid spin systems and opens new avenues for the design of versatile, temperature-responsive magnetoelectronic applications.

Magnetic heterostructures that combine antiferromagnetic (AFM) and ferromagnetic (FM) constituents are widely employed in commercial spintronic devices for sensing and data processing. Continuous research efforts focusing on the physical phenomena underlying the properties of these heterostructures have led to significant improvements of these devices as well as emerging application scenarios [1–10].

While the fully compensated magnetic moments of the AFM layer [11, 12] results in remarkable properties in its own, such as the absence of stray fields and terahertz (THz) spin dynamics [11–13], the key requirement for the functional properties of AFM/FM heterostructures is the coupling of the AFM and FM magnetic order [10, 14–19]. This coupling gives rise to functional magnetic phenomena, including shifts in the hysteresis loop, enhanced coercivity of the FM layer [14, 18, 19], rotational hysteresis under high magnetic fields [17], and rotatable anisotropy [20, 21]. The strength of this coupling can be modulated by adjusting the thickness of the FM or AFM layers [22–29]. In ferromagnetic resonance experiments, this interfacial coupling also produces effects such as unidirectional anisotropy, increased resonance linewidth, and shifts in the ferromagnetic resonance field and frequency [16, 22, 29–31].

Here we experimentally and theoretically demonstrate that the dependence of the AFM/FM coupling on the relative orientation of Néel vector and magnetization can be exploited to enable in-situ control of spin dynamics in  $\alpha$ -Fe<sub>2</sub>O<sub>3</sub>/Py heterostructures.

$\alpha$ -Fe<sub>2</sub>O<sub>3</sub> is an insulating antiferromagnet (AFM) with a corundum crystal structure [32–35], characterized by a Morin transition at approximately  $T_M \approx 260$  K [36, 37].

Above  $T_M$ ,  $\alpha$ -Fe<sub>2</sub>O<sub>3</sub> behaves as a canted antiferromagnet, exhibiting a small magnetic moment due to the Dzyaloshinskii–Moriya interaction, where the spins are oriented within the c-plane, perpendicular to the c-axis [34, 38]. Below  $T_M$ , the spins of  $\alpha$ -Fe<sub>2</sub>O<sub>3</sub> reorient along the c-axis, leading to the formation of a collinear antiferromagnet.

## RESULTS

We study heterostructures based on  $\alpha$ -Fe<sub>2</sub>O<sub>3</sub> single crystals and 10 nm-thick polycrystalline NiFe (Py) layers prepared by electron beam evaporation (see SI [39] for details on sample fabrication and  $\alpha$ -Fe<sub>2</sub>O<sub>3</sub> properties). To demonstrate the in-situ coupling control, we investigate the ferromagnetic resonance (FMR) behavior of the FM Py layer coupled to both canted and collinear phases of the  $\alpha$ -Fe<sub>2</sub>O<sub>3</sub> crystals. By varying the system temperature and AFM crystal orientation, we demonstrate that the AFM/FM spin-dynamics coupling can be exploited to control the FM resonance frequency via Néel-vector reconfiguration. Because the Néel-vector of  $\alpha$ -Fe<sub>2</sub>O<sub>3</sub> can be configured in-situ by magnetic fields and temperature, our findings present opportunities for tunable AFM/FM interactions in advanced magnetoelectronic devices.

In our experiments, we utilized AFM/FM heterostructures with a range of  $\alpha$ -Fe<sub>2</sub>O<sub>3</sub> crystal orientations. In the following, we refer to our heterostructures based on their crystal plane orientations: (11 $\bar{2}$ 0), (10 $\bar{1}$ 0), (1 $\bar{1}$ 02), and (0001) (see SI [39]).

The spin dynamics of the uniform FM resonance mode in these samples were studied using Cryogenic Ferromag-

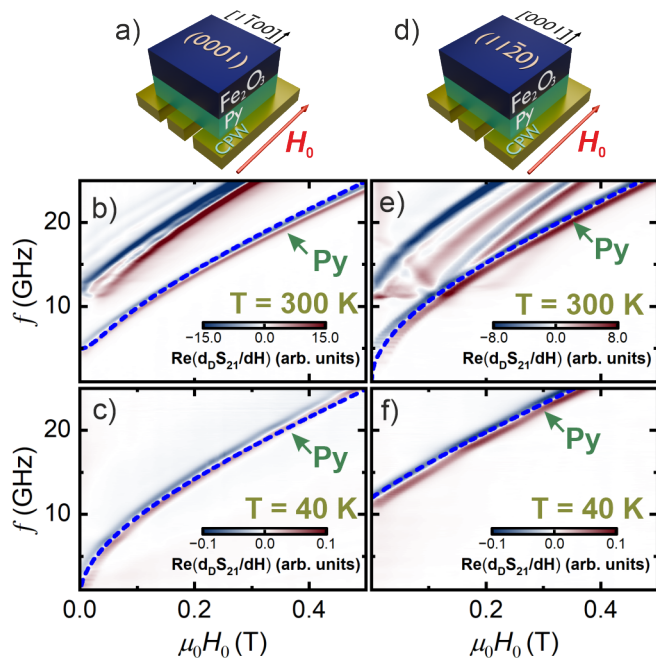


FIG. 1. (a) and (b) Schematic representation of the  $\alpha$ - $\text{Fe}_2\text{O}_3$ /Py heterostructures for the (0001) and (11 $\bar{2}$ 0) samples, respectively. The external magnetic field is applied in-plane for both samples. (c), (e) Real part of the background-corrected VNA signal for the (0001) sample at 300 K and 40 K, respectively. (d) and (f) display corresponding measurement results for the (11 $\bar{2}$ 0) sample, where  $H_0$  is applied in-plane and parallel to the [0001] axis. The dashed blue lines represent the Py resonance frequencies obtained from our model calculations (see text).

netic Resonance Spectroscopy (Cryo-FMR) based on an assembly of a coplanar waveguide connected to a Vector Network Analyzer (VNA) with 43 GHz bandwidth. The investigation was conducted by systematically varying the system temperature from 40 to 400 K.

Figure 1 presents schematics, experimental data and theoretical modeling for two selected  $\alpha$ - $\text{Fe}_2\text{O}_3$ /Py heterostructures to demonstrate the salient features of Néel-vector control of FM spin dynamics.

We first focus on results based on the (0001) heterostructure that is schematically depicted in Fig. 1(a). In Fig. 1(c), we show the FMR spectra and theoretical model obtained at 300 K - well above the Morin transition of  $\alpha$ - $\text{Fe}_2\text{O}_3$ . Specifically, we show the color-coded  $\text{Re}(d_D S_{21}/dH)$  spectra obtained by performing the derivative divide [40] data processing of our raw  $S_{21}$  VNA-FMR data. Multiple resonance lines above 10 GHz are observed and attributed to the magnetostatic quasi-FMR response of  $\alpha$ - $\text{Fe}_2\text{O}_3$ . These  $\alpha$ - $\text{Fe}_2\text{O}_3$  resonances are analyzed in more detail in the SI [39] and will not be discussed further here in order to focus on the Néel-vector control of the Py FMR instead. At lower frequencies, we observe a further single resonance line in panel (b) that

we attribute to the Py FMR response. Noteworthy is, that for  $H_0 \rightarrow 0$ , the FMR frequency is approximately  $f = 5$  GHz, while we would expect  $f \rightarrow 0$  for an isolated Py film [41, 42].

Conversely, Fig. 1(e) presents the FMR spectra recorded at 40 K, where the resonance mode of  $\alpha$ - $\text{Fe}_2\text{O}_3$  is well outside of the shown frequency range due to the transition of  $\alpha$ - $\text{Fe}_2\text{O}_3$  from canted AFM to collinear AFM. Importantly, we observe that the Py FMR frequency is now approaching  $f \rightarrow 0$  for  $H_0 \rightarrow 0$ . By comparing to panel (c) we furthermore observe that the Py resonance frequencies at 300 K and 40 K are similar at large  $H_0$ .

The right column of Fig. 1 shows the FMR spectra of the (11 $\bar{2}$ 0) heterostructure (see schematic depiction in panel (d)). Again, we recorded the spectra at temperatures above (e) and below (f)  $T_M$ , respectively. At 300 K, in contrast to our corresponding observations from the (0001) sample, we observe no enhancement of the Py resonance frequency for  $H_0 \rightarrow 0$ . Rather, for this heterostructure we now observe that the FMR spectra exhibit a clearly enhanced Py resonance frequency for all values of  $H_0$  which now assumes a value of  $f \approx 12$  GHz for  $H_0 = 0$  for  $T = 40$  K, again in contrast to the corresponding observations from the (0001) sample depicted in panel (c).

In summary, the experimental data in Fig. 1 strongly indicates that the Py magnetization dynamics reacts to the modification of  $\alpha$ - $\text{Fe}_2\text{O}_3$  Néel vector configuration that can be achieved by varying the temperature across the Morin transition and/or changing the interface orientation of  $\alpha$ - $\text{Fe}_2\text{O}_3$ .

## DISCUSSION

In Fig. 1, the blue dashed lines represent the result of theoretical modeling which is in agreement with the experimental observations. In the following, we will discuss our model to give an intuitive understanding of the underlying phenomena.

We assume a parallel interface coupling between the Néel vector ( $\mathbf{n}$ ) of  $\alpha$ - $\text{Fe}_2\text{O}_3$  and the Py magnetization vector ( $\mathbf{m}_F$ ) with the corresponding interface energy contribution  $w_{\text{int}} = -J_{\text{int}}\xi\mathbf{n} \cdot \mathbf{m}_F$ , where  $J_{\text{int}} > 0$  is the coupling strength and  $\xi$  is the effective thickness of the interface layer. Here we consider the uniform mode and neglect the inhomogeneous distribution of magnetic order within both Py and  $\alpha$ - $\text{Fe}_2\text{O}_3$ . We also exclude the excitation of the AFM dynamics by focusing on the effective anisotropy of Py induced by the interfacial coupling with  $\alpha$ - $\text{Fe}_2\text{O}_3$ . We also assume that the equilibrium orientation of the Néel vector does not depend on the cut and field value, and is either along the [0001] axis (below  $T_M$ ), or in the (0001) plane perpendicular to the external magnetic field (above  $T_M$ ) (see Fig. 1). In contrast, the equilibrium orientation of the Py magnetization depends

strongly on the orientation of the crystal cut as the stray fields always keep the Py magnetization in the film plane. It is calculated by minimizing the magnetic energy of the Py layer and the energy of the interfacial exchange coupling with the Néel vector. The full procedure is detailed in the SI [39].

Within this model, we find that for the (0001) sample above  $T_M$  (Fig.2 (b)), the Py magnetization vector is parallel to the Néel vector in absence of the magnetic field,  $\mathbf{n} \parallel \mathbf{m}_F$ . The interfacial coupling energy  $w_{\text{int}}$  in this case reaches the minimum value, thus maximizing the coupling. The external magnetic field  $\mathbf{H}_0 \parallel [1\bar{1}00]$  induces a gradual rotation of the Py magnetization away from  $\mathbf{n}$ , so that the effective coupling is reduced.

Below  $T_M$  (Fig.2 (a)), the Néel vector is aligned along the c-axis, perpendicular to both the sample plane and the Py magnetization. The application of an in-plane  $H_0$  has no effect on the equilibrium orientation  $\mathbf{m}_F$ , which always remains orthogonal to  $\mathbf{n}$ . As a result, in this case  $\mathbf{m}_F$  is decoupled from  $\mathbf{n}$ .

For the (11 $\bar{2}$ 0) sample we find a qualitatively different scenario. In contrast to the (0001) sample,  $\mathbf{n}$  and  $\mathbf{m}_F$  are completely decoupled above  $T_M$  (Fig.2 (d)), where  $\mathbf{m}_F \perp \mathbf{n}$ , and strongly coupled below  $T_M$ , where  $\mathbf{m}_F \parallel \mathbf{n}$ .

We interpret the interface coupling as an effective anisotropy field  $H_{\text{int}}(H_0)$  for the Py magnetization, which is reflected in the field dependence of the FMR frequency:

$$f(H_0) = \frac{\mu_0 \gamma}{2\pi} \sqrt{(H_{\text{int}}(H_0) + H_0)(M_F + H_0)}, \quad (1)$$

where  $\gamma$  is the gyromagnetic ratio of Py,  $\mu_0$  is the vacuum permeability and  $M_F$  is the saturation magnetization of Py. The strength of the anisotropy field  $H_{\text{int}}(H_0) = J_{\text{int}} \xi |\mathbf{n}| \cos \varphi_0(H_0) / d_F$  depends on the interface exchange coupling and thus decays with the thickness  $d_F$  of the Py layer. The angle  $\varphi_0$  between the equilibrium orientation of the Py magnetization and the Néel vector depends on the orientation of the cut and on the value of the magnetic field. For the perpendicular orientation  $\mathbf{n} \perp \mathbf{m}_F, \mathbf{H}_0$ ,  $\varphi_0 = \pi/2$  (Fig. 2(a) and (d)),  $H_{\text{int}} = 0$  and the FMR frequency follows the standard Kittel law resulting in the dashed blue lines in (Fig. 1(c) and (e)). In the case of  $\mathbf{n} \parallel \mathbf{m}_F \parallel \mathbf{H}_0$  (Fig. 2(c)),  $\varphi_0 = 0$  and  $f(H_0)$  dependence shows a gap  $\gamma \mu_0 \sqrt{H_{\text{int}} M_F}$ , which explains the enhanced Py resonance frequency reaching up to 12 GHz (Fig. 1(f)). In the intermediate case with  $\mathbf{n}, \mathbf{m}_F$ , and  $\mathbf{H}_0$  parallel to the interface (Fig. 2(b)) the angle  $\varphi_0$  changes from a non-zero equilibrium value at zero field to  $\varphi_0 = 0$  at saturation. This results in two distinct regions of  $f(H_0)$  (see Fig. 1(b)) below and above the saturation. For more details of the theoretical model we refer the reader to the SI [39].

Figure 3(a) shows the effective anisotropy field for vanishing external magnetic field  $H_{\text{int}}(H_0 = 0)$  that originates from interfacial coupling only, for both samples,

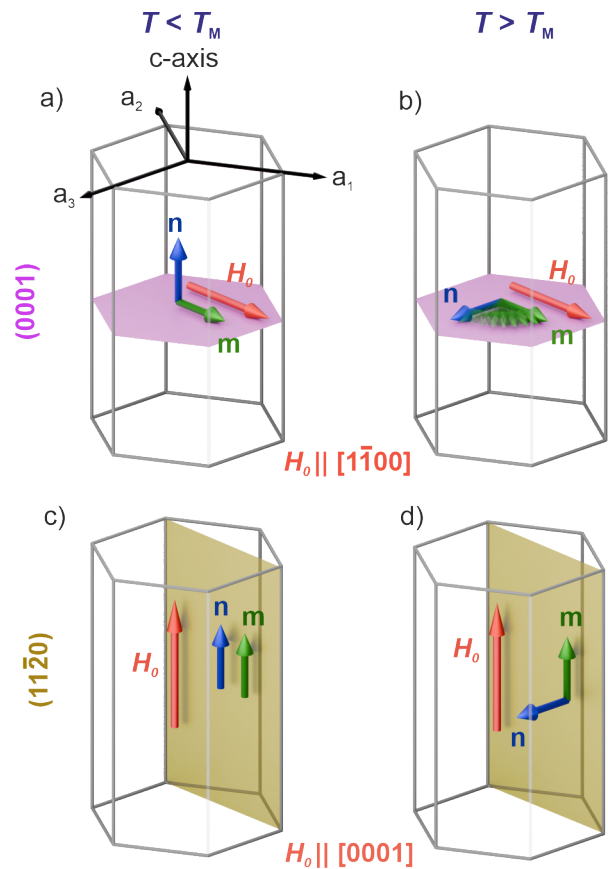


FIG. 2. Schematic depiction of the orientation of the Néel vector of  $\alpha\text{-Fe}_2\text{O}_3$  ( $\mathbf{n}$ , blue arrows) and magnetization vector of Py ( $\mathbf{m}_F$ , green arrows) below ((a) and (c)) and above ((b) and (d)) the Morin transition for different crystal cuts (shaded areas). Red arrows show the orientation of the external magnetic field. The competition of the Zeemann energy and the interfacial coupling with the Néel vector induces a reorientation of the Py magnetization while increasing the magnetic field for  $T > T_M$  and (0001) crystal cut as indicated by the transparent green arrows in panel (b).

measured across a temperature range from 40 K to 400 K. For the (0001) sample,  $H_{\text{int}}$  remains unchanged at temperatures well below  $T_M$ , indicating no modification in the spin configuration of the layers at the interface in agreement with the schematic of our model shown in Fig. 2(b). At approximately 220 K, an increase in  $H_{\text{int}}$  is observed, corresponding to the reorientation to parallel alignment of  $\mathbf{m}_F$  and  $\mathbf{n}$ , and the onset of the effective anisotropy induced by interfacial coupling.

Above this temperature,  $H_{\text{int}}$  increases sharply, reaching the saturation value  $\mu_0 H_{\text{int}} = 0.03$  T at 270 K.

In contrast, the (11 $\bar{2}$ 0) sample exhibits a maximum  $\mu_0 H_{\text{int}} = 0.15$  T at the lowest temperature  $T = 40$  K that we set in our experiments (cf. Fig. 2(d)). When increasing the temperature, near  $T_M$ , the value of  $H_{\text{int}}$  sharply drops and stays  $H_{\text{int}} \approx 0$  for  $T > T_M$ , indicating decoupling of the Py and  $\alpha\text{-Fe}_2\text{O}_3$  layers, as shown

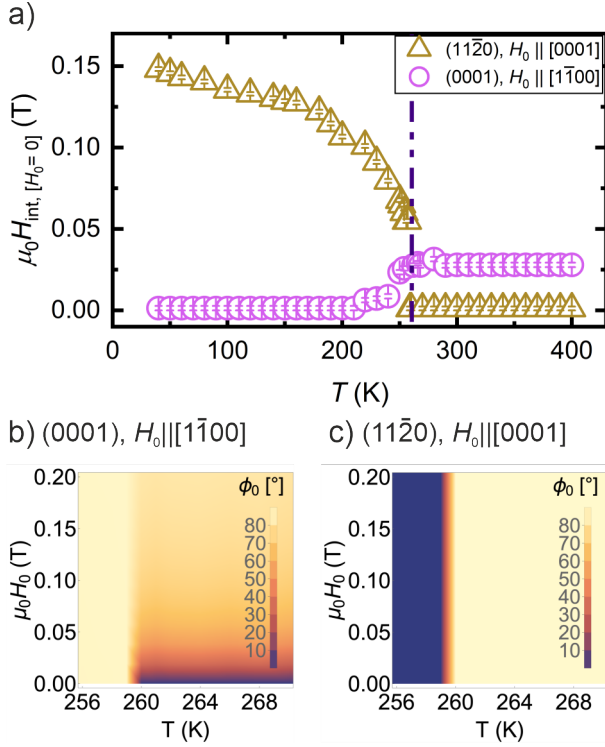


FIG. 3. a) The effective zero-field interfacial anisotropy,  $H_{\text{int}}(0 \text{ T})$ , was determined by fitting the FMR spectra (see Fig. 1) with Eq. (1) for the  $(11\bar{2}0)$  sample with  $H_0 \parallel [0001]$  (gold triangles) and  $(0001)$  sample with  $H_0 \parallel [1\bar{1}00]$  (magenta circles) over a range of temperatures from 40 to 400 K. b) and c) The equilibrium angle  $\varphi_0$  between the AFM Néel vector and the FM magnetization as a function of the applied static magnetic field and temperature for the  $(0001)$ -cut sample (b) and the  $(11\bar{2}0)$  sample (c).  $\varphi_0$  in panels b) and c) was calculated by using the experimentally determined interface exchange coupling strength. They show the complementary behavior of the  $(0001)$  and the  $(11\bar{2}0)$  sample. In each case there are two distinct regions with either low interface exchange coupling (nonzero  $\varphi_0$ ) or strong interface exchange coupling ( $\varphi_0 = 0$ ). Panel b) additionally showcases the saturation that occurs when the interface exchange coupling competes with the applied magnetic field.

in Fig. 2(c). In the intermediate temperature regime below  $T_M$ ,  $H_{\text{int}}$  smoothly decreases with increasing temperature. We attribute this to hybridization of the Py and  $\alpha\text{-Fe}_2\text{O}_3$  modes that is not captured in our didactic macrospin model.

We now discuss the impact of non-zero external magnetic fields  $H_0 > 0$  on  $H_{\text{int}}$  and thus the Py FMR frequency obtained from Eq.(1). To this end, Figure 3(b) and (c) show the relative orientation of Néel vector and magnetization  $\varphi_0$  as a function of temperature and  $H_0$  as obtained from our model. Figure 3(b) shows the case of the  $(0001)$  sample, where the applied magnetic field and the Néel vector are orthogonal (see Figure 2(a) and (b)). For low temperatures the  $(0001)$  sample shows zero  $H_{\text{int}}$  regardless of the strength of the applied field, as

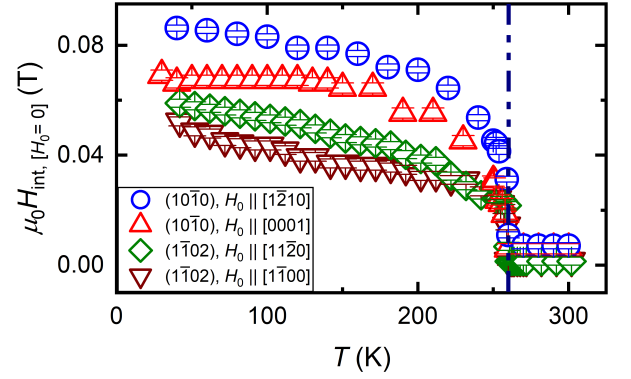


FIG. 4. The effective anisotropy  $H_{\text{int}}(0)$  for  $(10\bar{1}0)$  with  $H_0 \parallel [1\bar{2}10]$  (blue points),  $(10\bar{1}0)$  with  $H_0 \parallel [0001]$  (red points),  $(1\bar{1}02)$  with  $H_0 \parallel [11\bar{2}0]$  (green points), and  $(1\bar{1}02)$  with  $H_0$  projected along  $[1\bar{1}00]$  (brown points). The measurements were conducted over a temperature range of 40 to 300 K (see SI [39]).

the Néel vector lies perpendicular to the sample plane. Above the Morin transition the Néel vector lies in the sample plane, but perpendicular to the applied field. For low applied fields we observe  $\varphi_0 = 0$  and strong interface exchange coupling  $H_{\text{int}}$ . As the applied magnetic field is increased, the FM magnetization rotates away from the AFM Néel vector and into alignment with the applied magnetic field, reducing  $H_{\text{int}}$ .

Figure 3(c) shows the complementary case in the  $(11\bar{2}0)$  sample. Here, the applied field is parallel to the Néel vector below the Morin temperature (cf. Fig. 2(d)). Thus, we observe  $\varphi_0 = 0$  and strong interface exchange coupling  $H_{\text{int}}$  with concomitant enhanced Py resonance frequency for all applied field strengths in Fig. 1(f). Above the Morin temperature, the Néel vector again points out of the sample plane such that  $\varphi_0 = \pi/2$ . This results in vanishing  $H_{\text{int}}$  and unmodified Py resonance frequency.

To confirm our model, a systematic investigation was carried out using further  $\alpha\text{-Fe}_2\text{O}_3/\text{Py}$  systems with various  $\alpha\text{-Fe}_2\text{O}_3$  orientations. The external magnetic field was applied in two distinct in-plane directions (see SI [39]). The results demonstrate a systematic variation in the Py signal with changes in temperature, indicating that both the crystal orientation and temperature significantly influence the hybrid spin dynamics of the system.

Figure 4 presents the effective anisotropy,  $H_{\text{int}}$ , extracted from the fitting of the experimental data for the additional samples analyzed in this study. The samples exhibit behavior similar to that of the  $(11\bar{2}0)$  orientation with  $H \parallel [0001]$  (as shown in Fig. 3): strong coupling below  $T_M$  with  $H_{\text{int}}$  reaching maximum value at 40 K, and zero coupling above  $T_M$ . Switching between the coupled and decoupled regime is controlled by the temperature induced reorientation of the Néel vector. These findings confirm that the strength of  $H_{\text{int}}$  in  $\alpha\text{-Fe}_2\text{O}_3/\text{Py}$  het-

erostructures is governed by both the crystal structure of  $\alpha$ -Fe<sub>2</sub>O<sub>3</sub> and temperature.

In conclusion, our investigation of spin dynamics in  $\alpha$ -Fe<sub>2</sub>O<sub>3</sub>/Py heterostructures reveals the critical role of the relative orientation of Néel vector and magnetization for spin dynamics in AFM/FM heterostructures. By utilizing cryogenic ferromagnetic resonance spectroscopy, we explored the spin dynamics behavior of these heterostructures as a function of temperature and crystal orientation. Our findings demonstrate that the interfacial coupling strength is highly sensitive to both the crystal orientation of  $\alpha$ -Fe<sub>2</sub>O<sub>3</sub> and temperature, particularly near  $T_M$ . Our model highlights the importance of the relative alignment between the Néel vector in  $\alpha$ -Fe<sub>2</sub>O<sub>3</sub> and the magnetization vector in Py as key determinants of the exchange interaction strength. These results provide valuable insights into the manipulation of spin dynamics in AFM/FM heterostructures, offering potential applications in the design of advanced spintronic devices that leverage temperature-tunable exchange coupling. The ability to control the resonance frequency and interfacial coupling strength through precise temperature and orientation adjustments presents promising opportunities for future developments in magneto-electronics.

## METHODS

**Sample preparation.** Natural bulk  $\alpha$ -Fe<sub>2</sub>O<sub>3</sub> crystals, with dimensions of  $10 \times 10 \times 1 \text{ mm}^3$ , were commercially obtained from SurfaceNet GmbH. The crystals were oriented along different main crystallographic planes—(0001), (1 $\bar{1}$ 02), (11 $\bar{2}$ 0), and (10 $\bar{1}$ 0)—with various in-plane orientations (see Supplementary Information [39]). Prior to deposition, the surfaces were plasma-etched to remove organic contaminants. A 10 nm-thick permalloy (Py) layer was deposited onto the main plane of each crystal using molecular beam epitaxy. To prevent oxidation of the Py layer, a 3 nm-thick aluminum oxide capping layer was applied. Both deposition processes were performed under high-vacuum conditions.

**Spectroscopy measurements.** FMR measurements of the stacks were conducted using an optimized setup with a vector network analyzer capable of frequency-sweep measurements from 10 MHz to 43.5 GHz and an external magnetic fields up to 0.5 T. Measurements were performed over a temperature range of 40 K to 400 K under high-vacuum conditions of  $10^{-7}$  mbar. The system temperature was varied in larger increments between 40 K and 250 K, and between 270 K and 400 K, with finer increments near the Morin temperature to obtain higher-resolution data. The external magnetic field was applied in-plane to the samples along two orthogonal directions separated by  $90^\circ$ , and was swept from +0.5 T

to  $-0.5$  T in 3 mT steps. At each magnetic field increment, the frequency was swept from 1 GHz to 40 GHz to record the FMR spectra. Measurements were conducted with a power level of  $-10$  dBm. The real and imaginary components of the complex scattering parameter  $S_{21}$  were recorded. A frequency-dependent background was removed using a derivative divide method, as described in [43]. Additional information can be found in the SI [39].

**Model.** Equilibrium orientation of the Néel vector and Py magnetization are calculated from minimization of the magnetic energy of the bilayer. This includes the magnetic anisotropy energy density of  $\alpha$ -Fe<sub>2</sub>O<sub>3</sub>,  $w_{\text{AF}}$  [44], of Py,  $w_F$ , and the energy of the interface exchange coupling by  $w_{\text{int}}$ . Our parameters are listed in Table S1 of the SI [39].

$$w_{\text{AF}} = M_S \left( -\frac{1}{2} \bar{H}_{2\parallel}(T) n_z^2 - \frac{H_{\text{DMI}}}{H_{\text{ex}}} \vec{n} \cdot (\vec{H} \times \hat{z}) \right)$$

$$w_F = \frac{1}{2} \mu_0 M_F^2 (\hat{m}_F \cdot \hat{e})^2 - M_F \hat{m}_F \cdot \vec{H}, \quad (2)$$

$$w_{\text{int}} = -J_{\text{int}} \xi M_S M_F \delta(\hat{e} \cdot \mathbf{r}) \hat{m}_F \cdot \hat{n}, \quad (3)$$

where  $M_S/2$  is the saturation magnetization of the magnetic sublattice in the AFM,  $H_{\text{DMI}} > 0$  is the homogeneous DMI field that leads to a small spin canting and finite magnetization in the easy-plane phase. The out-of-plane anisotropy  $\bar{H}_{2\parallel}(T)$  assumes different values depending on the temperature  $T$ , such that it is positive below the *Morin* temperature and changes sign at the *Morin* transition.  $H_{\text{ex}}$  is the AFM exchange field,  $\hat{e}$  defines the normal to the film plane (depends on the cut).

The FMR resonant frequency is calculated from the standard LLG equations for Py magnetization linearized around the given equilibrium state. We fit the experimentally obtained data and use our theoretical modeling to extract the interface exchange coupling strength from the zero field frequency gap of the Py signal. Using the value from this estimation we can numerically replicate the experimentally observed spectrum and determine the FM magnetization's and AFM Néel vector's ground state orientation in presence of interface exchange coupling. More details on the model can be found in the SI [39].

We acknowledge financial support by the Deutsche Forschungsgemeinschaft (DFG, German Research Foundation) within the Transregional Collaborative Research Center TRR 173/3-268565370 ‘‘Spin+X’’ (Projects B15, B13 and B11). O.G. and T.W. also acknowledge support from Deutsche Forschungsgemeinschaft (DFG) SPP 2137, project number 403233384. M.W. acknowledges support from the European Research Council (ERC) under the European Union’s Horizon Europe research and innovation program (Grant agreement No. 101044526).

H.A. and M.W. contributed to the experimental idea. H.A. performed the experiments, the experimental data post processing and generated the figures containing experimental data. T.W. provided the theoretical model, the data analysis and fitting of the experimental data to the theoretical model and the theory-related figures. H.A., P.S., and G.K. performed the low-temperature measurements. L.S., M.D., and M.Y. contributed to the samples fabrication and characterization. H.A. and T.W. prepared the manuscript. O.G., V.V., P.P. and M.W. provided the scientific leadership of the project and helped with proofreading the manuscript. All authors discussed the results and commented on the paper.

---

\* E-Mail: h.alhamdo@rptu.de; These authors contributed equally.

† These authors contributed equally.

- [1] Li, K. *et al.* Exchange coupling and its applications in magnetic data storage. *J. Nanosci. Nanotechnol.* **7**, 13–45 (2007).
- [2] Chappert, C., Fert, A. & Van Dau, F. N. The emergence of spin electronics in data storage. *Nat. Mater.* **6**, 813–823 (2007).
- [3] Dieny, B. *et al.* Giant magnetoresistive in soft ferromagnetic multilayers. *Physical Review B* **43**, 1297 (1991).
- [4] Nogués, J. & Schuller, I. K. Exchange bias. *J. Magn. Magn. Mater.* **192**, 203–232 (1999).
- [5] Skumryev, V. *et al.* Beating the superparamagnetic limit with exchange bias. *Nature* **423**, 850–853 (2003).
- [6] Nguyen, A. T. *et al.* Magnetoresistive performances in exchange-biased spin valves and their roles in low-field magnetic sensing applications. *J. Adv. Mater* **3**, 399–405 (2018).
- [7] Huang, Y.-H. *et al.* A spin-orbit torque ratchet at ferromagnet/antiferromagnet interface via exchange spring. *Adv. Funct. Mater.* **32**, 2111653 (2022).
- [8] Lau, Y.-C., Betto, D., Rode, K., Coey, J. & Stamenov, P. Spin-orbit torque switching without an external field using interlayer exchange coupling. *Nat. Nanotechnol* **11**, 758–762 (2016).
- [9] Železný, J., Wadley, P., Olejník, K., Hoffmann, A. & Ohno, H. Spin transport and spin torque in antiferromagnetic devices. *Nat. Phys* **14**, 220–228 (2018).
- [10] Takano, K., Kodama, R., Berkowitz, A., Cao, W. & Thomas, G. Interfacial uncompensated antiferromagnetic spins: Role in unidirectional anisotropy in polycrystalline Ni<sub>81</sub>Fe<sub>19</sub>/CoO bilayers. *Phys. Rev. Lett.* **79**, 1130 (1997).
- [11] Néel, L. Propriétés magnétiques de l'état métallique et énergie d'interaction entre atomes magnétiques. *Ann. Phys.* **11**, 232–279 (1936).
- [12] Nagamiya, T., Yosida, K. & Kubo, R. Antiferromagnetism. *Adv. Phys.* **4**, 1112 (1955).
- [13] Rezende, S. M., Azevedo, A. & Rodríguez-Suárez, R. L. Introduction to antiferromagnetic magnons. *J. Appl. Phys.* **126** (2019).
- [14] Meiklejohn, W. H. & Bean, C. P. New magnetic anisotropy. *Phys. Rev.* **102**, 1413 (1956).
- [15] Finazzi, M. Interface coupling in a ferromagnet/antiferromagnet bilayer. *Phys. Rev. B* **69**, 064405 (2004).
- [16] McMichael, R. D., Stiles, M. D., Chen, P. & Egelhoff Jr, W. F. Ferromagnetic resonance studies of nio-coupled thin films of ni 80 fe 20. *Phys. Rev. B* **58**, 8605 (1998).
- [17] Schlenker, M. C. Étude des pertes par hystérésis oscillante dans des couches minces multiples avec couplage ferro-antiferromagnétique. *J. Phys. Colloq.* **29**, C2–157 (1968).
- [18] Lamirand, A. D. *et al.* Robust perpendicular exchange coupling in an ultrathin CoO/PtFe double layer: Strain and spin orientation. *Phys. Rev. B* **88**, 140401 (2013).
- [19] Mishra, S. *et al.* Dual behavior of antiferromagnetic uncompensated spins in NiFe/IrMn exchange biased bilayers. *Phys. Rev. B* **81**, 212404 (2010).
- [20] Prosen, R., Holmen, J. & Gran, B. Rotatable anisotropy in thin permalloy films. *J. Appl. Phys.* **32**, S91–S92 (1961).
- [21] Lommel, J. & Graham Jr, C. Rotatable anisotropy in composite films. *J. Appl. Phys.* **33**, 1160–1161 (1962).
- [22] Al-Hamdo, H., Wagner, T. *et al.* Coupling of ferromagnetic and antiferromagnetic spin dynamics in Mn<sub>2</sub>Au/NiFe thin film bilayers. *Phys. Rev. Lett.* **131**, 046701 (2023).
- [23] Kohlhepp, J. & de Jonge, W. Influence of the fm/afm interface morphology on the exchange coupling in epitaxial Co (001)/fct-Mn (001). *J. Appl. Phys.* **95**, 6840–6842 (2004).
- [24] Jung, H., Traistaru, O. & Fujiwara, H. Effect of the kinds of ferromagnetic layers on exchange coupling strength in IrMn/FM films. *J. Appl. Phys.* **95**, 6849–6851 (2004).
- [25] Singh, A. K. & Chandra, R. Thickness dependent interfacial magnetic coupling in [La<sub>2</sub>NiMnO<sub>6</sub>/LaMnO<sub>3</sub>] multilayers. *J. Magn. Magn. Mater.* **448**, 180–185 (2018).
- [26] Beiranvand, A. & Liedke, M. O. Tuned AFM-FM coupling by the formation of vacancy complex in Gd<sub>0.6</sub>Ca<sub>0.4</sub>MnO<sub>3</sub> thin film lattice you may also like tuned AFM-FM coupling by the formation of vacancy complex in Gd<sub>0.6</sub>Ca<sub>0.4</sub>MnO<sub>3</sub> thin film lattice. *J. Condens. Matter Phys* **33**, 9 (2021).
- [27] Pokhil, T., Song, D. & Linville, E. Magnetic force microscope study of antiferromagnet-ferromagnet exchange coupled films. *J. Appl. Phys.* **91**, 6887–6889 (2002).
- [28] Beik Mohammadi, J. *et al.* Broadband ferromagnetic resonance characterization of anisotropies and relaxation in exchange-biased IrMn/CoFe bilayers. *Phys. Rev. B* **95**, 064414 (2017).
- [29] Stoecklein, W., Parkin, S. & Scott, J. Ferromagnetic resonance studies of exchange-biased permalloy thin films. *Phys. Rev. B* **38**, 6847 (1988).
- [30] Scott, J. Ferromagnetic resonance studies in the bilayer system Ni<sub>0.80</sub>Fe<sub>0.20</sub>/Mn<sub>0.50</sub>Fe<sub>0.50</sub>: Exchange anisotropy. *J. Appl. Phys.* **57**, 3681–3683 (1985).
- [31] Speriosu, V., Parkin, S. & Wilts, C. Standing spinwaves in FeMn/NiFe/FeMn exchange-bias structures. *IEEE Trans. Magn.* **23**, 2999–3001 (1987).
- [32] Curry, N., Johnston, G., Besser, P. & Morrish, A. Neutron diffraction measurements on pure and doped synthetic hematite crystals. *Philos. Mag.* **12**, 221–228 (1965).
- [33] Besser, P., Morrish, A. & Searle, C. Magnetocrystalline anisotropy of pure and doped hematite. *Phys. Rev.* **153**, 632 (1967).

- [34] Muench, G., Arajs, S. & Matijević, E. The morin transition in small  $\alpha$ -Fe<sub>2</sub>O<sub>3</sub> particles. *Phys. Status Solidi A* **92**, 187–192 (1985).
- [35] Chevallier, R. Propriétés magnétiques de l’oxyde ferrique rhomboédrique Fe<sub>2</sub>O<sub>3</sub> $\alpha$ . *J. phys. radium* **12**, 172–188 (1951).
- [36] Morin, F. Magnetic susceptibility of  $\alpha$ -Fe<sub>2</sub>O<sub>3</sub> and  $\alpha$ -Fe<sub>2</sub>O<sub>3</sub> with added titanium. *Phys. Rev.* **78**, 819 (1950).
- [37] Guiland, C. Magnetic properties of iron oxide  $\alpha$ -Fe<sub>2</sub>O<sub>3</sub>. *J. Phys. Radium* **12**, 489 (1951).
- [38] Schroer, D. & Nininger Jr, R. Morin transition in  $\alpha$ -Fe<sub>2</sub>O<sub>3</sub> microcrystals. *Phys. Rev. Lett.* **19**, 632 (1967).
- [39] See *SI at URL for details about the sample preparation, modeling, experimental techniques and evaluation, and additional data, which includes References [33, 36, 44]*.
- [40] Maier-Flaig, H. *et al.* Note: Derivative divide, a method for the analysis of broadband ferromagnetic resonance in the frequency domain. *Rev. Sci. Instrum.* **89** (2018).
- [41] Zhao, Y. *et al.* Experimental investigation of temperature-dependent gilbert damping in permalloy thin films. *Sci. Rep.* **6**, 22890 (2016).
- [42] Klemmer, T., Ellis, K. & Van Dover, B. Ferromagnetic resonance frequency of a thin mo-permalloy film. *J. Appl. Phys.* **87**, 5846–5848 (2000).
- [43] Weiler, M. *et al.* Helimagnon resonances in an intrinsic chiral magnonic crystal. *Phys. Rev. Lett.* **119**, 237204 (2017).
- [44] Lebrun, R. *et al.* Long-distance spin-transport across the Morin phase transition up to room temperature in ultra-low damping single crystals of the antiferromagnet  $\alpha$ -Fe<sub>2</sub>O<sub>3</sub>. *Nat. Commun.* **11**, 6332 (2020).